Front. Chem. Sci. Eng. 2024, 18(8): 89
https://doi.org/10.1007/s11705-024-2442-0

RESEARCH ARTICLE

Bimetallic reduced graphene oxide/zeolitic imidazolate framework hybrid aerogels for efficient heavy metals removal

Nurul A. Mazlan, Allana Lewis, Fraz Saeed Butt, Rajakumari Krishnamoorthi, Siyu Chen, Yi Huang (✉)

School of Engineering, Institute for Materials & Processes, The University of Edinburgh, Edinburgh EH9 3FB, UK

Abstract Graphene oxide is a promising adsorption material. However, it has been difficult to recycle and separate graphene oxide in the solution. To alleviate this problem, graphene oxide was thermally reduced to produce porous hydrogel which was then functionalized with polydopamine. The functional groups act as not only adsorption sites but also nucleation sites for *in situ* crystallization of cobalt-doped zeolitic-imidazolate-framework-8 nano-adsorbents. The effects of cobalt-doping contents on the physicochemical and adsorption properties of the resulting aerogel were also evaluated by varying the cobalt concentration. For instance, the reduced graphene oxide-polydopamine/50cobalt-zeolitic-imidazolate-framework-8 aerogel exhibited a high surface area of 900 $m^2 \cdot g^{-1}$ and maintained the structure in water after ten days. The as-synthesized aerogels showed an ultrahigh adsorption capacity of 1217 ± 24.35 $mg \cdot g^{-1}$ with a removal efficiency of > 99% of lead, as well as excellent adsorption performance toward other heavy metals, such as copper and cadmium with adsorption capacity of 1163 ± 34.91 and 1059 ± 31.77 $mg \cdot g^{-1}$, respectively. More importantly, the lead adsorption stabilized at 1023 ± 20.5 $mg \cdot g^{-1}$ with a removal efficiency of > 80% after seven cycles, indicating their potential in heavy metal removal from industrial wastewater.

Keywords rGO, Co-doped ZIF-8, heavy metals, adsorption, aerogel

1 Introduction

The growth of industries, including mining, electroplating, battery production, and leather processing, has resulted in significant releases of wastewater contaminated with heavy metals into aquatic environments [1]. Many heavy metal ions exhibit carcinogenic, non-biodegradable, mutagenic, and bio-accumulative properties. Hence, consuming water containing heavy metals such as Pb(II), Cd(II), and Cu(II) can cause diseases such as pulmonary, immunological, and endocrine disorders and cancers [2]. To address this issue, the adsorption technique is among the water treatment techniques that have been widely applied due to its cost efficiency, alleviating secondary pollution, and low energy consumption [3]. Activated carbon [4], and natural fibers [5] are some examples of typical adsorbents that have been extensively investigated for the removal of pollutants such as heavy metals from industrial effluent. However, at very high or low pH values, these adsorbents frequently show poor specific areas or instability. These resulted in a significant reduction of heavy metal adsorption performance.

Aerogel materials have emerged as promising adsorbent materials for heavy metal adsorption. The key benefits of aerogel-based adsorbents include adjustable surface chemistry, low density, high specific surface area, and loose porous structure. Aerogels have been reported to demonstrate exceptional adsorption capacity, effectively capturing and immobilizing heavy metal ions from aqueous solutions [6]. The critical parameter in the development of aerogel is the selection of the materials. In addition, customization of the surface chemistry of aerogels through functionalization allows for improved selectivity, making them more effective in discriminating between different metal ions during the adsorption process. Moreover, the development of hybrid materials, combining the advantages of aerogels with other nanomaterials, synergistically enhances adsorption capacities and overall efficiency.

Recently, graphene oxide (GO), one of the carbon nanomaterials distinguished by its outstanding and unique

Received November 4, 2023; accepted March 5, 2024; online May 20, 2024

E-mail: Yi.Huang@ed.ac.uk

properties, has garnered considerable attention for its environmental applications. Because of its remarkable mechanical strength, relatively large specific area, and abundant oxygen functional groups, GO is considered a promising material for the preconcentration of heavy metal ions [7]. Nonetheless, despite its excellent properties, GO-based adsorbents still have significant drawbacks. For instance, the propensity of GO to aggregate due to interplanar π–π bonds results in the reduction of adsorption between GO layers [8]. Moreover, the challenge of separating GO from aqueous solutions is attributed to its low specific weight, hydrophilicity, and dispersibility causes secondary pollution. These challenges limit their applicability in wastewater treatment. To overcome this issue, the construction of three-dimensional (3D) adsorbents that serve as a robust scaffold imparting mechanical stability to the material via the assembly of low-dimensional carbon nanomaterials, such as GO, has been recognized as a promising strategy. This approach aims to create convenient and high-efficiency adsorbents for environmental applications.

One method is to construct a 3D GO structure from two-dimensional (2D) nanosheets via a reduction method. The reduction of the oxygen-containing group on the skeleton of graphene in the presence of a chemical-reducing agent leads to the formation of 2D material. Here, the 2D layered structure with numerous conjugated domains can self-assemble into a 3D structure via simple van der Waals and hydrogen bonding interactions forming hydrogel [9]. However, following the reduction process, the reduced GO (rGO) has considerably fewer oxygen functional groups and possibly low surface area, adversely affecting adsorption performance. Hence, increasing the type and quantities of functional groups, e.g., those with chelating abilities, might be essential. Among these, polydopamine (PDA) has garnered increasing attention recently, mainly due to the resemblance of its structure to 3,4-dihydroxyl-L-phenylalanine. This structure is a critical component of the mussel foot protein known for its strong chelating and adhesion abilities [10].

Interestingly, these functional groups can also serve as nucleation sites for *in situ* growth of guest materials. Recently, many studies have been reported on developing GO nanocomposites, such as GO/metal-organic-framework (MOF) to enhance the properties and adsorption performance [11]. GO/MOF-based composites are particularly promising due to the possibility of achieving a synergic effect between the porous solid of MOF (high surface area and abundant adsorption sites) and GO (excellent chemical and mechanical stability).

Zeolitic imidazolate frameworks (ZIFs), one subclass of MOF, consist of tetrahedral transition metal ions bridged by imidazole derivatives [12]. ZIFs are of great interest due to their excellent physical and chemical properties, such as crystallinity, porosity, high surface area, and exceptional chemical and thermal stability. One of the crucial features is that Zn(II) ions can be substituted by Co(II) or Cu(II) ions without altering their topology [12]. Kaur et al. [13] first reported the synthesis of bimetallic Co-Zn ZIF-8 and found that the bimetallic ZIFs have a higher surface area than the parent crystals. Shortly after that, Zaręba et al. [14] reported a mixed-metal strategy to alter the size and the physicochemical properties of the obtained heterometallic structure. Therefore, it is deduced that Co doping holds significance for several reasons. Firstly, Co doping can alter the physicochemical properties of ZIF-8, potentially leading to modifications in its structural and surface characteristics. This alteration may result in an increased surface area, providing more active sites for adsorption. Secondly, introducing cobalt into ZIF-8 can impart additional functionalities and reactivity to the material, influencing its performance in specific applications. In particular, cobalt's known affinity for heavy metals suggests that Co-doped ZIF-8 may exhibit improved capability in selectively attracting and adsorbing heavy metal ions from solutions, enhancing its utility in water treatment or other environmental remediation processes. Despite the excellent properties and tuning abilities of ZIFs, the direct application of preferred nanosized material in environmental applications has been cautious due to the difficulties in adsorbent separation and regeneration. Specifically, MOF powder exhibits invasive characteristics owing to its nanoscale particle sizes. Consequently, retrieving MOFs and recovering the powder from treated water is challenging and could result in secondary pollution. Therefore, there has been a huge demand for more advanced adsorbents prepared with more sustainable and environmentally considerate approaches.

In this work, we report a facile fabrication strategy of hybrid aerogels with a hierarchical structure rGO-PDA/Co-doped ZIF-8 with enhanced adsorption sites and large surface area. The 3D rGO structure was constructed via the assembly of 2D GO nanosheets by thermal reduction. Subsequently, the 3D rGO aerogel undergoes surface modification with PDA. Then, the surface of the aerogel was decorated with Co-doped ZIF crystals. The influence of Co doping levels on the properties of aerogels was evaluated. Full adsorption potential was analyzed at different heavy metal initial concentrations, and the ability of the aerogel to adsorption of different types of heavy metals was also evaluated. Notably, the performance of the aerogel for the adsorption of Pb(II) was examined under different pH conditions. Overall, the membrane exhibits excellent adsorption performance and good recyclability; the mechanisms of adsorption are discussed. The combination of ZIFs with a 3D graphene-based structure not only integrated their advantages and mitigated the shortcomings of the individual components but also benefited from the macroscopic 3D hybrid structure in terms of adsorbent separation and recovery.

2 Experimental

2.1 Materials

GO 1% dispersion was purchased from William Blythe. Zinc nitrate hexahydrate ($Zn(NO_3)_2 \cdot 6H_2O$, 98%), $Co(NO_3)_2 \cdot 6H_2O$ (97.7%), 2-methylimidazole (99%), L-ascorbic acid (99%), lead(II) nitrate (99%), cadmium nitrate tetrahydrate (98%) and copper(II) sulfate (99%), magnesium chloride (99%), sodium chloride (99%), were purchased from Sigma Aldrich. Dopamine hydrochloride ($C_8H_{11}NO_2 \cdot HCl$, 99%) and tris-HCl (1 $mol \cdot L^{-1}$) were obtained from Alfa Aesar. 1-Propanol (99%) was purchased from Thermo Fischer.

2.2 Synthesis of rGO hydrogel

Firstly, 10 $mg \cdot mL^{-1}$ stock GO solution was diluted with deionized water to attain 2 $mg \cdot mL^{-1}$ GO suspension, followed by an hour of ultrasonication. Subsequently, 0.1 g of ascorbic acid was introduced into the prepared GO solution and subjected to an additional 30 min of sonication to ensure thorough mixing. The solution was then placed into a Teflon-coated autoclave and heated at 120 °C for three hours. After heat treatment, the resultant rGO hydrogel was extensively rinsed with deionized water to eliminate any residual ascorbic acid. The hydrogel was then preserved in deionized water for subsequent steps.

2.3 Synthesis of PDA-coated rGO hydrogel

The acquired rGO hydrogel was immersed in a solution containing dopamine hydrochloride at a concentration of 2 $mg \cdot mL^{-1}$, dissolved in a 10 $mmol \cdot L^{-1}$ tris-HCl buffer. The mixture was stirred at 25 °C for a duration of 2 h. Subsequently, the rGO-coated PDA hydrogel underwent multiple rinses with deionized water. The hydrogel was then allowed to air-dry at ambient temperature overnight.

2.4 *In situ* synthesis of rGO-PDA/Co-ZIF-8 aerogel

The synthesized rGO-PDA hydrogel was submerged in a solution with specified concentrations of $Zn(NO_3)_2 \cdot 6H_2O$ and $Co(NO_3)_2 \cdot 6H_2O$ and subjected to stirring for six hours. Following this, the hydrogel was immersed in a separate container filled with 0.40 $mmol \cdot L^{-1}$ of 2-methylimidazole solution and 8 mL of 1-propanol, also under stirring conditions, for another 6 h. Subsequently, the prepared hydrogel underwent multiple washes and was subjected to freeze-drying for 24 h, resulting in the formation of the rGO-PDA/Co-ZIF-8 aerogel.

2.5 Characterizations

The structural characteristics of the fabricated samples were investigated using a JEOS JSM-IT100 scanning electron microscope (SEM). Elemental composition analysis was conducted using a Zeiss 400 Compact SEM (Germany) equipped with an Oxford Instruments (UK) energy dispersive X-ray spectroscopy (EDS) system, utilizing an accelerating voltage of 5 kV. X-ray diffraction (XRD) measurements were performed on a Bruker D8 Advance system using Cu Kα radiation over a 2θ range from 4.0° to 50.0°. Fourier transform infrared (FTIR) spectroscopy data were acquired within the wavelength range of 500 to 4000 cm^{-1} to investigate the chemical bonding throughout the material's synthesis process. Thermal stability assessments were conducted using thermogravimetric analysis (TGA) and differential scanning calorimetry (DSC), where the aerogel samples were heated at a rate of 10 $°C \cdot min^{-1}$ in a nitrogen atmosphere. The TGA/DSC measurements spanned a temperature range from 25 to 800 °C. Nitrogen adsorption/desorption isotherms were recorded at 77 K on an autosorb iQ from Quantachrome to evaluate microporosity and surface area, applying the Brunauer-Emmett-Teller (BET) method. Prior to the BET analysis, samples underwent degassing in a N_2 atmosphere at 120 °C for 8 h to eliminate any loosely attached water and other volatiles. Micropore volumes were assessed using the t-plot method across a relative pressure (P/P_0) range of 0.05 to 0.3. The total pore volume was calculated from the isotherm's desorption branch at $P/P_0 = 0.97$, with mesopore volume derived by subtracting micropore volume from the total. X-ray photoelectron spectroscopy (XPS) analysis was performed on a Scienta ESCA 300 instrument with a monochromated aluminum Kα X-ray source. The concentration of heavy metals before and after adsorption was quantified using an inductively coupled plasma-optical emission spectrometer (ICP-OES), specifically a Perkin Elmer Optima 8300 DV. Zeta potential measurements were made using a zeta potentiometer to assess the material's surface charge properties.

2.6 Heavy metal adsorption

In this study, lead(II) nitrate, cadmium nitrate tetrahydrate, and copper(II) sulfate were selected to assess the adsorption efficiency of the synthesized rGO-PDA/Co-ZIF-8 aerogels. For the adsorption tests, 0.03 g of aerogel was added to 200 mL of each heavy metal solution, prepared at specific initial concentrations and pH levels. After 5 h of adsorption, the samples were then retrieved for analysis.

2.6.1 Percentage of heavy metal removal and adsorption capacity

The adsorption capacity ($mg \cdot g^{-1}$) and the percentage heavy metal removal efficiency (%) were calculated by using Eqs. (1) and (2), respectively.

$$\text{Adsorption capacity } (q_e) = \frac{(C_0 - C_e)V}{m}, \tag{1}$$

$$\text{Dye removal efficiency } (\%) = \frac{C_0 - C_t}{C_0} \times 100, \tag{2}$$

q_e represents the adsorption capacity at equilibrium ($\text{mg}\cdot\text{g}^{-1}$), while C_0, C_e, and C_t, denote the concentrations of the heavy metal in the solution at the start, at equilibrium, and at a given time point, respectively, expressed in $\text{mg}\cdot\text{L}^{-1}$. The term V refers to the volume of the heavy metal solution in liters, and m signifies the weight in grams of the aerogel used.

2.6.2 Kinetic study

The adsorption behavior of the synthesized material was examined using the pseudo-first-order (PFO) and pseudo-second-order (PSO) kinetic models, which are articulated in Eqs. (3) and (4), respectively [15].

$$\ln(q_e - q_t) = \ln(q_e) - K_1 t, \tag{3}$$

$$\frac{t}{q_t} = \frac{1}{K_2 q_e^2} + \frac{1}{q_e} t. \tag{4}$$

The equilibrium adsorption capacity, denoted as q_e ($\text{mg}\cdot\text{g}^{-1}$), is the adsorption capacity at time t, represented as q_t ($\text{mg}\cdot\text{g}^{-1}$). Additionally, there are rate constants, K_1 and K_2, corresponding to PFO and PSO kinetics, respectively, with units of min^{-1} and $\text{g}\cdot\text{mg}^{-1}\cdot\text{min}^{-1}$. The variable t represents time, measured in minutes.

2.6.3 Adsorption isotherms

To elucidate the underlying adsorption mechanism, the adsorption isotherm was analyzed through the application of both Langmuir and Freundlich isotherm models, represented by Eqs. (5) and (6), respectively [15].

$$\frac{C_e}{q_e} = \frac{1}{q_{\max}} C_e + \frac{1}{K_1 q_{\max}}, \tag{5}$$

$$\ln(q_e) = \ln(K_F) + \frac{1}{n} \ln(C_e). \tag{6}$$

where q_e denotes the adsorption capacity at equilibrium ($\text{mg}\cdot\text{g}^{-1}$), C_e signifies the concentration of the heavy metal at equilibrium ($\text{mg}\cdot\text{L}^{-1}$), $q_{\max}$ represents the maximum capacity for monolayer adsorption, K_1 is the Langmuir constant ($\text{L}\cdot\text{mg}^{-1}$), and K_F refers to the constant of the Freundlich isotherm ($\text{mg}\cdot\text{g}^{-1}$).

3 Results and discussion

3.1 The synthesis of 3D rGO-PDA/Co-ZIF-8

The fabrication process of the 3D rGO-PDA/Co-ZIF-8 aerogel is depicted through a schematic in Fig. 1 based on our previous work [15]. The synthesis commenced with the formation of a 3D rGO hydrogel through the hydrothermal reduction of GO nanosheet dispersions in an acidic medium. Specifically, 0.1 g of ascorbic acid was

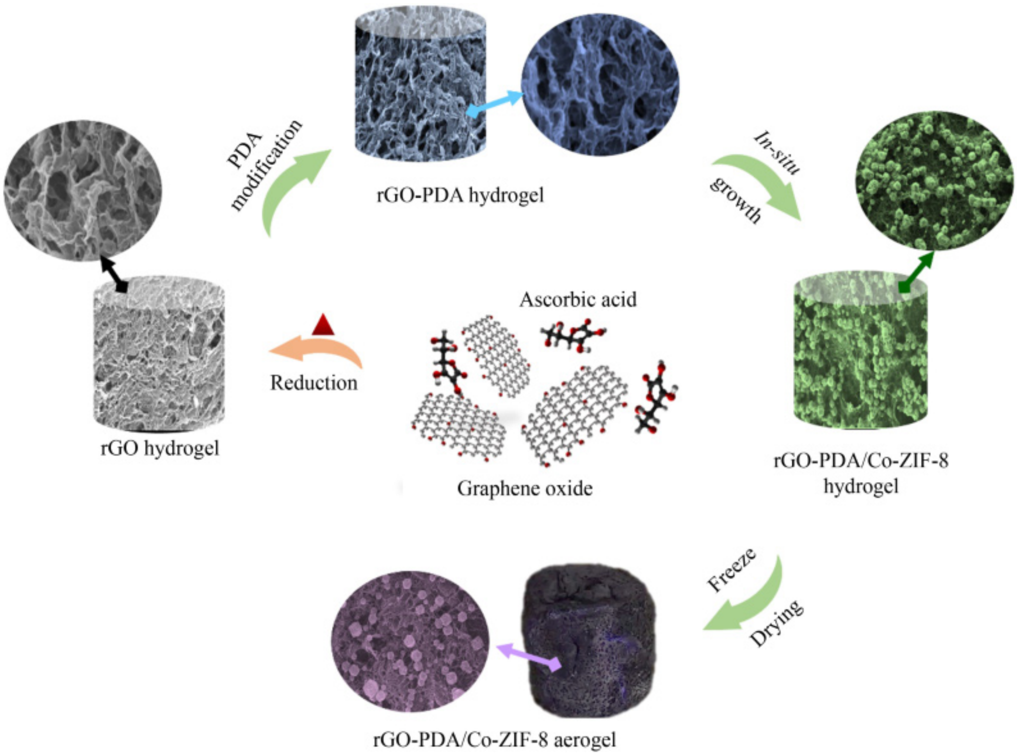

Fig. 1 Schematic illustration of the fabrication process of bimetallic rGO-PDA/Co-ZIF-8 hybrid aerogel.

introduced into a 2 mg·mL^{-1} GO dispersion, followed by heating at 120 °C for three hours. This thermal reduction facilitated the elimination of hydrophilic functional groups such as hydroxyl (–OH) and carboxyl (–COOH), promoting enhanced π–π stacking interactions among the 2D graphene layers [16]. Such interactions led to the sequential self-assembly of rGO nanosheets, leading to the formation of a monolithic rGO hydrogel structure. Subsequently, this hydrogel was immersed in a PDA solution for two hours, allowing surface functionalization through the self-polymerization of dopamine, resulting in the deposition of a PDA layer on the rGO structure. Dopamine, with its functional groups—catechol, amine, and imino—readily forms bonds with nanomaterials like rGO through covalent and non-covalent interactions, establishing a cross-linked network featuring π–π stacking on the rGO framework [17]. Following surface modification, the rGO-PDA hydrogel was thoroughly rinsed to remove excess PDA and air-dried at ambient conditions overnight. The rGO-PDA surface was decorated with bimetallic nano-adsorbent by stirring the hydrogel in a solution containing predetermined quantities of $Zn(NO_3)_2·6H_2O$ and $Co(NO_3)_2·6H_2O$ at ambient temperature for a duration of 6 h. During this procedure, the positively charged zinc and cobalt ions were attracted and bound to the negatively charged rGO-PDA hydrogel framework through electrostatic attraction, resulting in the formation of a rGO-PDA/Co^{2+}/Zn^{2+} composite hydrogel. Notably, an interaction known as cation-π also played a role, where the metal cations interacted with the graphitic planes of the rGO, facilitating the connection between adjacent rGO nanosheets and thus bolstering the mechanical stability within the layers [18]. Subsequently, this composite hydrogel was subjected to agitation in a 2-methylimidazole solution at ambient temperature, leading to the selective formation of bimetallic Co-ZIF-8 nano-adsorbents through the reaction of the pre-bound cobalt and zinc ions with the 2-methylimidazole ligands. It is worth noting the ZIF-8 nanocrystals are incorporated owing to their promising adsorption capabilities (see Fig. S1 (cf. Electronic Supplementary Material, ESM) for characterizations and adsorption properties of ZIF-8). The newly formed rGO-PDA/Co-ZIF-8 hydrogel was then extensively rinsed with deionized water to eliminate any residual, unreacted ligands. The synthesis was finalized by lyophilizing the rGO-PDA/Co-ZIF-8 hydrogel for 24 h, resulting in the production of the aerogel form of rGO-PDA/Co-ZIF-8.

3.2 Characterizations of the hydrogel samples at each fabrication step

To examine the changes in morphology and structure, samples fabricated at each stage of synthesis were analyzed using XRD, FTIR spectroscopy, nitrogen adsorption-desorption, and TGA coupled with DSC (TGA-DSC). This section specifically highlights the synthesis of rGO-PDA/50Co-ZIF-8. According to Fig. 2(a), the initial GO sample exhibited a characteristic diffraction peak at $2\theta = 10.2°$, consistent with previously reported GO samples [19]. The reduction of GO led to a significant decrease in the initial diffraction peak, with a new, broader peak emerging at $2\theta = 24.5°$. This indicates the formation of a denser rGO structure due to the removal of oxygen-containing groups. Following the rapid application of PDA, this peak shifted to a slightly lower angle of $2\theta = 23.9°$, suggesting the intercalation of PDA among the rGO layers [20]. Subsequent *in situ* formation of cobalt-doped ZIF-8 and freeze-drying resulted in an aerogel displaying diffraction peaks at 7.0°, 10.0°, 12.2°, 14.2°, 15.9°, 17.4°, 24.4°, and 25.7°. These peaks align well with those characteristics of ZIF-8 and ZIF-67, confirming the successful synthesis of Co-doped ZIF-8 nano-adsorbents through *in situ* crystallization [21].

The alteration in chemical composition and functional groups due to surface modification with dopamine and the subsequent formation of Co-ZIF-8 were analyzed through FTIR spectroscopy, as depicted in Fig. 2(b). Initial analysis of the GO sample revealed distinct absorption bands at 1044, 1618, 1735, and 3389 cm^{-1}, which correspond to the stretching vibrations of C–O, C=C, C=O, and O–H, respectively [22]. After the reduction process, there was an observable enhancement in the peak intensity for C=C at 1590 cm^{-1}, while the peaks for C–O, C=O, and O–H at 1355, 1732, and 3389 cm^{-1}, respectively, showed a reduction in intensity, indicating the removal of some functional groups [23]. The PDA functionalization introduced new absorption peaks within the 1010 to 1040 cm^{-1} range for C–O stretching vibrations. Additionally, the appearance of peaks at 1551 and 1630 cm^{-1}, corresponding to C=C and C=N stretching modes, signified the incorporation of aromatic amine structures in the rGO. The emergence of a peak at 3184 cm^{-1}, attributed to secondary amine formation, further validated the successful integration of PDA within the rGO matrix.

This transformation in the FTIR spectrum between rGO and rGO-PDA samples suggests a significant interaction between rGO and PDA. Initially, the integration of rGO within the PDA during its polymerization led to the elimination of the peak associated with C=O stretching [24]. Additionally, π–π interactions between the benzene rings of PDA and the rGO framework shifted the C=C absorption band from 1591 to 1551 cm^{-1}, indicating strong adherence of PDA to the rGO surface. Following the *in situ* synthesis of Co-doped ZIF-8 crystals, new absorption peaks at 993 and 1562 cm^{-1} were identified, indicative of C–N and C=N bonds, respectively. Peaks within the 1100 to 1400 cm^{-1} range corresponding to C–N stretching, and a peak in the 420 to 425 cm^{-1} range, related to Zn–N and Co–N bonds, were also observed, confirming the successful creation of Co-doped ZIF-8

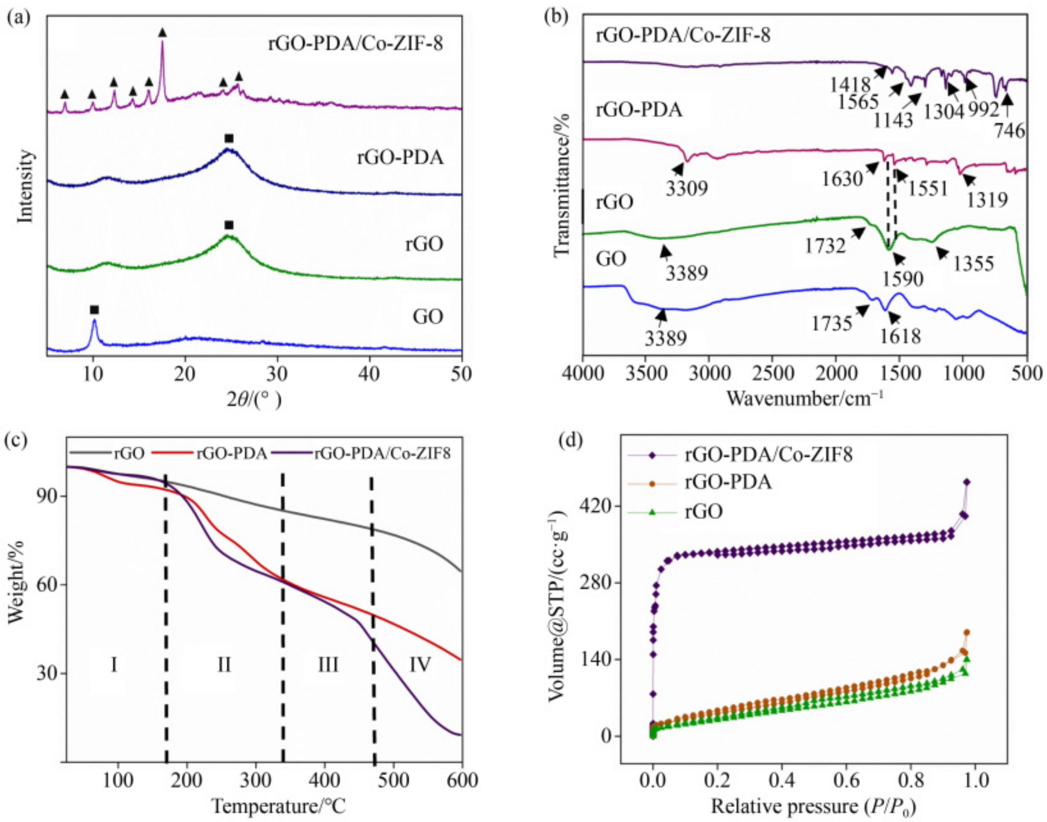

Fig. 2 Aerogel characterization: (a) XRD pattern spectra at various stages of aerogel preparation, (b) FTIR spectra at various stages of aerogel preparation, (c) TGA curve of rGO-PDA/50Co-ZIF-8 aerogel, and (d) N_2 adsorption-desorption isotherm of rGO, rGO-PDA, rGO-PDA/50Co-ZIF-8 aerogel.

crystals on the PDA-rGO surface [25]. These FTIR findings are consistent with the XRD analysis, collectively affirming the effective PDA functionalization and *in situ* generation of cobalt-doped ZIF-8.

Subsequently, the alterations in the thermal properties of the samples were extensively investigated through TGA analyses which were conducted in a nitrogen environment at a heating rate of 10 °C·min^{-1} for a temperature range of 25–600 °C. The TGA profiles of the rGO, rGO-PDA, and rGO-PDA/50Co-ZIF-8 samples are illustrated in Fig. 2(c). The weight loss observed in all samples can be categorized into four phases: Phase I (25–180 °C), Phase II (180–320 °C), Phase III (320–450 °C), and Phase IV (320–450 °C). Notably, the incorporation of each component affected the overall thermal stability of the as-synthesized aerogel. The rGO sample displayed a steady weight loss of 14 wt % across the four phases, attributed to the decomposition of oxygen functional groups and the carbonization of the carbon skeleton. In Phase I, both rGO-PDA and rGO-PDA/50Co-ZIF-8 samples exhibited weight losses ranging from 5 to 8 wt % primarily attributable to moisture evaporation [16]. In Phase II, a rapid weight loss of 20 and 22 wt % was observed for rGO-PDA and rGO-PDA/50Co-ZIF-8 samples due to the carbonization of PDA [26]. It is worth mentioning that the rGO-PDA/50Co-ZIF-8 sample exhibited a slightly higher weight loss compared to the rGO-PDA sample. This is attributed to the volatilization of chemically adsorbed water during the synthesis of Co-ZIF-8. Further weight loss was noticed in Phase III for both rGO-PDA and rGO-PDA/50Co-ZIF-8 samples. More specifically, rGO-PDA/50Co-ZIF-8 demonstrated a higher weight loss of 20 wt % compared to the 15 wt % observed for rGO-PDA. The weight loss exhibited by the rGO-PDA sample is associated with the further carbonization of stable functional groups such as carboxyl from PDA. Meanwhile, the weight loss exhibited by the rGO-PDA/50Co-ZIF-8 sample is attributed to the carbonization of PDA and the rupture of the Co-ZIF-8 structure as well as the carbonization of 2-methylimidazole [19]. All materials continued to lose weight in the final phase due to the slow carbonization of the skeleton of rGO [27].

One of the crucial characteristics of the high-efficiency adsorbent is the surface area. Therefore, BET analysis was utilized to examine the alteration in the specific surface area of the sample at each fabrication stage. The N_2 adsorption isotherm of rGO, rGO-PDA, and rGO-PDA/50Co-ZIF-8 samples are presented in Fig. 2(d). All three aerogels showed the presence of mesopores structure indicated by a typical IV isotherm accompanied by the hysteresis loop. The rGO sample demonstrated a surface area of 80 m^2·g^{-1}. Following the surface modification with PDA, the rGO-PDA sample exhibited a slightly enhanced surface area of 120 $m^2 \cdot g^{-1}$. According to the *t*-plot data, both rGO and rGO-PDA displayed minimal micropore volume, suggesting that the surface area of these samples was predominantly contributed by mesoporous structures. Through Barrett-Joyner-Halenda calculation, it was observed that the incorporation of PDA into the rGO structure led to a significant increase in mesopore volume from 0.124 to 0.241 $mL \cdot g^{-1}$. Remarkably, the rGO-PDA/50Co-ZIF-8 aerogel exhibited an enhanced surface area of 900 $m^2 \cdot g^{-1}$ when compared to both rGO and rGO-PDA samples. Additionally, its micropore volume increased to 0.604 $mL \cdot g^{-1}$, while there was a notable rise in mesopore volume to 0.54 $mL \cdot g^{-1}$ due to the *in situ* crystallization of Co-doped ZIF-8 within its structure. Consequently, the incorporation of microporous Co-doped ZIF-8 nanoparticles within the rGO-PDA aerogel led to the formation of a more intricate porous framework with an extensive surface area [28]. As a result, it can be confidently asserted that the improved structural characteristics render the rGO-PDA/50Co-ZIF-8 aerogel a promising adsorbent when compared to the intermediate samples, namely rGO and rGO-PDA, prepared in this study.

Ultimately, XPS analysis was carried out on the rGO, rGO-PDA, and rGO-PDA/50Co-ZIF-8 aerogels to elucidate their experimental composition at particular binding energy levels (eV). The complete spectrum of the samples is presented in Fig. S2(a) (cf. ESM). In particular, the rGO exhibited prominent peaks at ~200 and ~500 eV, corresponding to C 1s and O 1s elements, respectively. Following functionalization with PDA, an additional peak at ~400 eV corresponding to N 1s emerged, accompanied by the intensification of C 1s and O 1s. Subsequent to the *in situ* growth of Co-ZIF-8, two new peaks ascribed to the Co 2p and Zn 2p elements emerged at ~800 and ~1000 eV, respectively. This occurred simultaneously with the elevated N 1s peak, providing additional confirmation of the successful synthesis of Co-ZIF-8 within the aerogel structure. The high resolution of scans of each component was further elucidated in detail in Figs. S2(b–f). In summary, the XPS results were in good agreement with XRD, FTIR, and TGA results which all suggested that a strong interaction existed between each component, thus forming a robust hierarchical porous structure.

3.3 Synthesis of the rGO-PDA/Co-ZIF-8 aerogels with varied Co dopings

To get a clear observation of the local hydrogel structure at each step of the fabrication step, all samples were studied using SEM and shown in Fig. 3. As shown in Fig. 3(a), the as-synthesized rGO aerogel displayed a hierarchical porous structure with an interconnected porous network resembling sponge-like substance. Following the surface functionalization with PDA, the network structure showed a relatively rougher and wrinkled surface compared with rGO aerogels (Fig. 3(b)) indicating that rGO surfaces are covered by self-polymerized PDA layers. Notably, after the *in situ* growth of ZIF-8, the surface becomes decorated with dodecahedral nanocrystals with varying sizes depending on the concentration of cobalt (0%Co-, 30%Co-, 50%Co-, 70%, and 100%Co-doped ZIF-8) (Figs. 3(c–f) and S3 (cf. ESM)). From the SEM images of the Co-doped ZIF-8 nanocrystals on the aerogel surface, it can be observed that an increase in Co concentration resulted in the formation of larger crystals. In contrast, without the presence of Co, nanocrystals are formed with an average size of 140 ± 56 nm (Figs. 3(c) and S3(a)). By simply introducing Co, the Co-doped ZIF-8 crystal size increased to 160 ± 26, 220 ± 16, 285 ± 11, and 367 ± 47 nm, for 30%, 50% 70%, and 100% of Co, respectively (Figs. 3(g–i), S3(b) and S3(c)). It is suggested that the increase in nanocrystal size was owing to the incorporation of cobalt(II) salt in the synthesis which favored crystal growth rather than nucleation [14]. It is also worth mentioning that the incorporation of Co^{2+} ions into the ZIF-8 framework did not alter the ZIF-8 chemical structure due to comparable ionic radii of Co^{2+} (0.72 Å) and Zn^{2+} (0.74 Å) [13]. Therefore, the Co-doped ZIF-8 crystals maintain the ZIF-8 and ZIF-67 crystal structure (Figs. 3(c) and S1). Furthermore, the embedding of Co-ZIF-8 did not alter the porous rGO-PDA aerogel network structure. However, the aerogel surface became rugged and rich in defects due to the particles formed both above and below the thin rGO layers.

To further evaluate the composition and distribution of cobalt and zinc elements in the structure of Co-doped ZIF-8 nanocrystals, the surface of the aerogel decorated with different concentrations of Co-doped ZIF-8 was analyzed with EDS mapping (Fig. S4, cf. ESM). The weight percentage of the two elements (Co/Zn) from the EDX spectrum was summarized in Table S1 (cf. ESM). Figures S4(a–c) showed the EDS analysis of rGO-PDA/ZIF-8 aerogel. The EDX spectrum showed only the presence of zinc in the structure of the imidazolate framework, thus, confirming pure ZIF-8 crystals. Upon the addition of 30% molar of cobalt in the ZIF-8 synthesis recipe, the EDS mapping displayed the coexistence of cobalt and zinc with 37% of cobalt and 63% of zinc (Figs. S4(d–f)). As the Co doping molar concentration increased up to 50%, the EDS mapping of rGO-PDA/50Co-ZIF-8 aerogel exhibited a similar distribution of zinc and cobalt in the ZIF structure (Figs. S4(g) and S4(h)). In addition, the EDX spectrum further confirmed 50/50 cobalt and zinc in the structure (Fig. S4(i)). Further increasing the Co doping percentage up to 70%, the EDS mapping of rGO-PDA/70Co-ZIF-8 aerogel showed more cobalt present in the ZIF structure compared to zinc (Figs. S4(j) and S4(k)). The EDX spectrum also displayed the presence of 72% cobalt and 28% zinc (Fig. S4(l)).

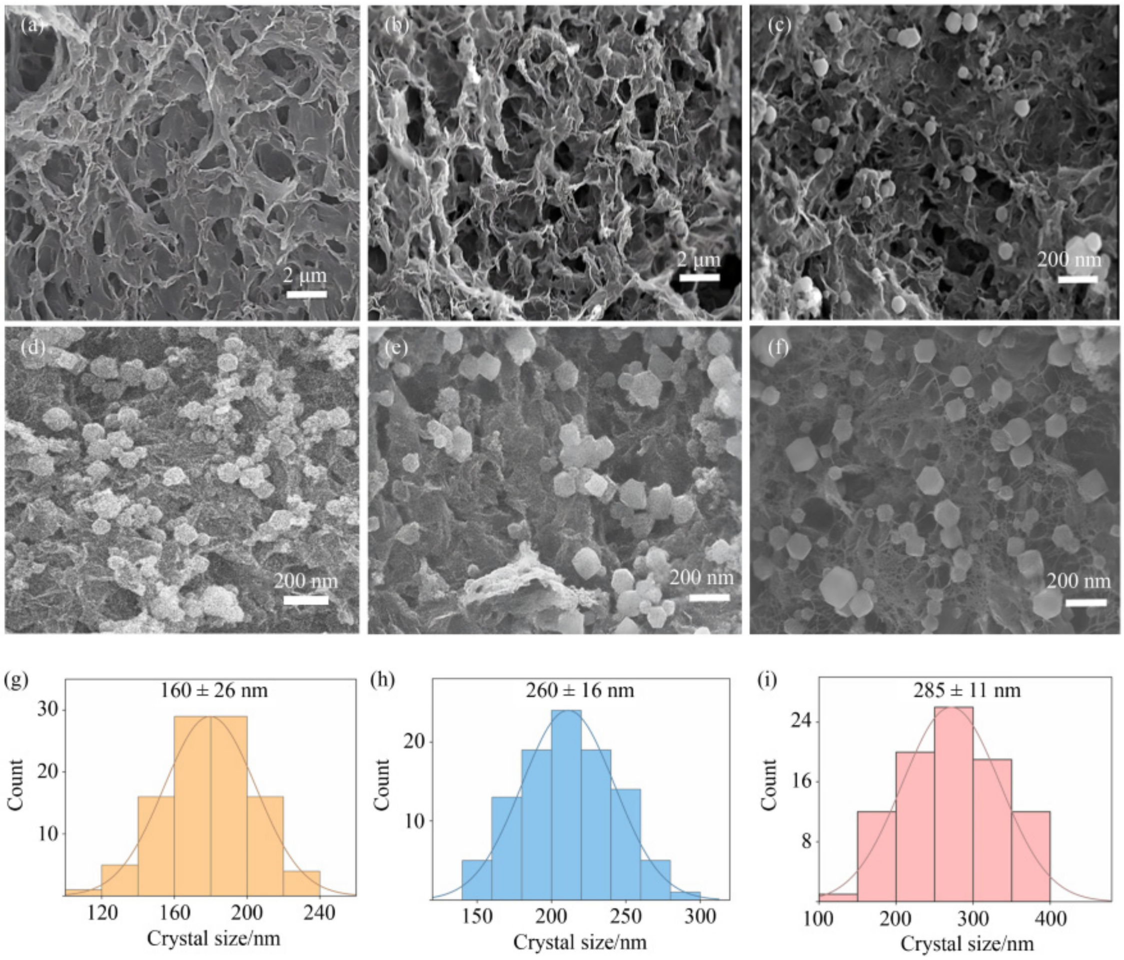

Fig. 3 SEM images of the as-synthesized aerogels: (a) rGO, (b) rGO-PDA, (c) rGO-PDA/ZIF-8, (d) rGO-PDA/30Co-ZIF-8, (e) rGO-PDA/50Co-ZIF-8, and (f) rGO-PDA/70Co-ZIF-8. Crystal size distribution on the surface of aerogel at different Co doping concentrations: (g) 30%, (h) 50% Co, and (i) 70%Co. The sizes of the crystals were estimated using ImageJ software.

Figure S4(m–o) showed only the presence of cobalt in the imidazolate structure confirming the ZIF-67 pure crystals on the aerogel if only Co was used in the synthesis. Overall, the EDS mapping analysis revealed the coexistence of zinc and cobalt elements in the ZIF-8 samples that were prepared in a bimetallic system. The above results also confirmed the successful incorporation of cobalt in the ZIF-8 structure.

As has been reported previously, the properties of ZIF material such as specific surface area can be tweaked after the addition of other metal elements in the structure [13,14,25]. Therefore, in this study, the properties of the aerogel with different Co doping were evaluated using BET analysis (Fig. 4(a) and Table S2 (cf. ESM)). Interestingly, the cobalt-doped aerogel exhibited higher surface area compared to the aerogels decorated with pure crystals ZIF-67. More specifically, rGO-PDA/ZIF-8 showed a surface of 850 $m^2 \cdot g^{-1}$, the specific surface area further increased to 875 and 900 $m^2 \cdot g^{-1}$ for rGO-PDA/30Co-ZIF-8 and rGO-PDA/50Co-ZIF-8 aerogel, respectively. However, further increasing the Co-dopings, the specific surface area decreased to 861 and 815 $m^2 \cdot g^{-1}$, for rGO-PDA/70Co-ZIF-8 and rGO-PDA/ZIF-67 aerogels, respectively. Therefore, it can be deduced that a certain amount of Co doping could increase the porosity of the crystals as inferred from the enhancement of the surface area. This result is in agreement with previous studies of bimetallic Co-Zn ZIFs [13,14]. The XRD pattern of the aerogels with different percentages of Co-doping crystals are presented in Fig. 4(b). rGO-PDA/ZIF-8 aerogel exhibits weak diffraction peaks at 7.1°, 10.1°, 12.3°, 14.3°, 16.1°, 24.1°, and 26.2° fit with the characteristic peaks of ZIF-8 at the actual XRD pattern. Since ZIF-8 and ZIF-67 have similar crystal structures due to the ionic radii of Co(II) and Zn(II) in tetrahedral coordination are quite comparable (0.74 Å for Zn(II) and 0.72 Å for Co(II)) [29]. Therefore, the positions of diffraction peaks of the cobalt-doped crystals aerogels showed a very close agreement to the XRD patterns of the aerogel with ZIF-8 structure. Additionally, Fig. 4(c) displayed the FTIR patterns of all aerogel samples. As shown in the figure, all the aerogel samples exhibit similar FTIR peak patterns. The signal peaks at 1147 and 759 cm^{-1} were associated with C–N and out-of-plane

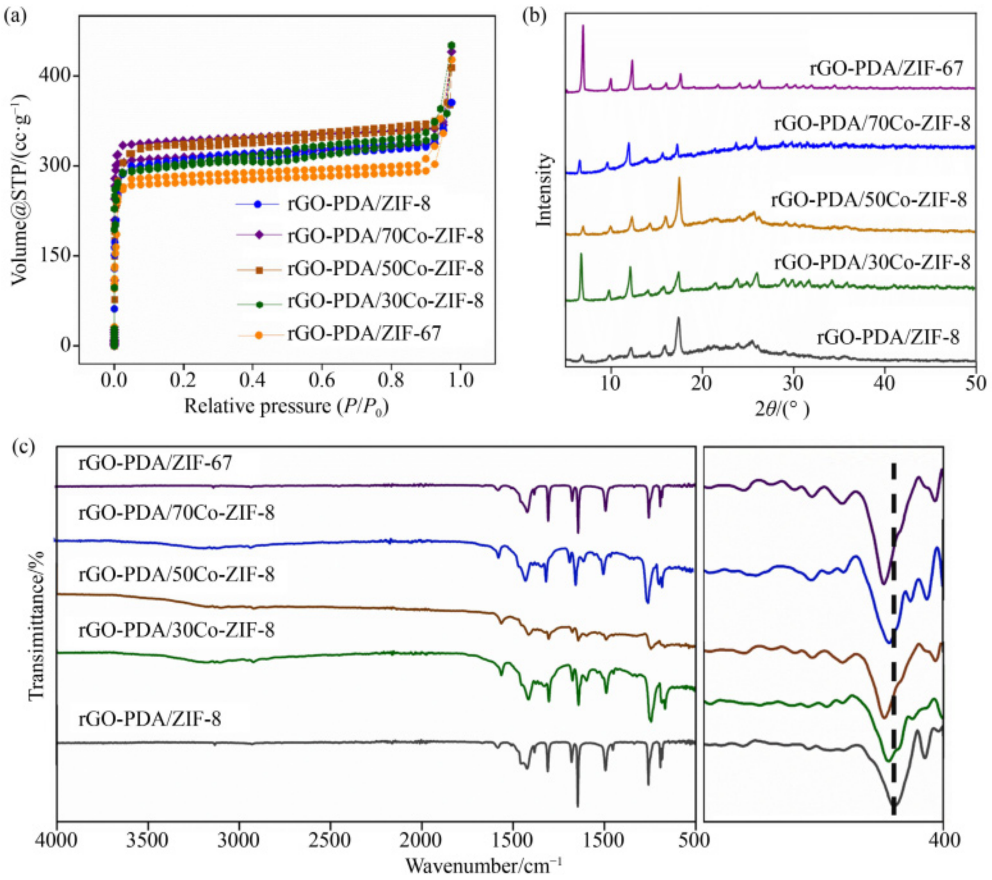

Fig. 4 Characterization of different cobalt doping aerogel: (a) BET analysis, (b) XRD patterns, and (c) FTIR.

bending of the imidazole ring, respectively. The peak between 421 and 425 cm^{-1} is associated with the Zn–N and Co–N bond. The emergence of C–N, Zn–N, and Co–N bonds indicated that the Co-/Zn ZIF has been decorated into the structure of rGO-PDA aerogel [30].

3.4 Formation mechanism and water stability of rGO-PDA/Co-ZIF-8 aerogels

The formation process of the rGO-PDA/Co-ZIF-8 aerogel is depicted in Fig. S5 (cf. ESM). As previously described, the initial step involved the creation of a 3D rGO structure through hydrothermal reduction of GO. This process eliminated hydrophilic groups, thereby strengthening the π–π stacking interaction among the rGO nanosheets, leading to the self-assembly of the nanosheets into an rGO hydrogel. Upon PDA modification, a robust π–π interaction occurred between the aromatic ring of rGO and PDA, resulting in the extensive wrapping of PDA onto the rGO aerogel structure. This interaction was corroborated by FTIR analysis (Fig. 2(b)), which revealed spectral shifts and the disappearance of the C–O bond. This observation was consistent with XPS analysis (Fig. S2), which demonstrated the emergence of new peaks associated with π–π bonding and the complete disappearance of the O–C=O peak. When the rGO-PDA aerogel was immersed in a solution containing zinc and cobalt ions, the electrostatic forces between these metal ions and the negatively charged PDA and rGO oxygen functional groups facilitated the rapid adsorption of metal ions onto the structure. Subsequently, upon immersion in a 2-methylimidazole solution, the metal ions selectively reacted with the ligand molecules, leading to the formation of cobalt-doped ZIF-8 crystals on the rGO-PDA sample's structure.

To evaluate the stability of the as-synthesis aerogels in an aqueous solution, and determine the optimum Co doping in the aerogel that not only has excellent structure properties but also good stability in an aqueous solution, water stability tests were performed on the rGO-PDA/Co-ZIF-8 aerogels with varied Co dopings. First, the as-synthesized aerogels were immersed in deionized water for ten days. The aerogel structure and crystallinity of the crystals were then examined with XRD and SEM (Fig. 5). The XRD pattern of the aerogels after exposure to water is presented in Fig. 5(a). Notably, the rGO-PDA/ZIF-8, rGO-PDA/30Co-ZIF-8, and rGO-PDA/50Co-ZIF-8 aerogel still maintained the characteristic diffraction peaks associated with ZIF-8/ZIF-67. This suggested that the crystals can survive even after ten days in water conditions, demonstrating good hydrostability. On the other hand, rGO-PDA/70Co-ZIF-8 and rGO-PDA/ZIF-67 aerogels displayed a completely different XRD diffraction pattern because of the likely crystal decomposition in the aqueous solution. The structure of the aerogels after water immersion was further studied with SEM (Figs. 5(b–f)). As shown in Figs. 5(b–d), most of the ZIF-8 crystals as well as those doped with 30% and 50% cobalt still preserved the original dodecahedral crystal structure with no weight loss observed before and after immersion in aqueous solution. In contrast, crystals with 70% Co-doping exhibited irregular, defective surfaces (Fig. 5(e)), accompanied by weight loss of 0.08 g. Meanwhile, ZIF-67 completely lost the original crystal structure due to its low hydrostability in water conditions which was further proved by the weight loss of 0.11 g, the highest among aerogels studied (Fig. 5(f)). Therefore, the SEM observation and mass analysis were consistent with the XRD studies. The stability of the aerogel at different pH conditions was studied by immersing the aerogel at pH 4, 7, and 9 for ten days. The mass loss as the result of the aerogel's degradation was evaluated by recording the mass before and after adsorption for each day (Fig. S6, cf. ESM). It is noted that the aerogel shows the highest degradation in acidic conditions at pH 4 with a mass loss of ~15%. On the other hand, the aerogel exhibited mass loss of ~2%–3% in neutral and alkaline pH conditions. Based on the above results, rGO-PDA/50Co-ZIF-8 aerogel showed the highest surface area, while still maintaining good stability in water, which was critically important to its long-term heavy metal adsorption performance (see Section 3.5.1 Effect of Co dopings and operating conditions on the adsorption performance and Section 3.6).

3.5 Heavy metal adsorption

3.5.1 Effect of Co dopings and operating conditions on the adsorption performance

Nowadays, the discharge of wastewater containing heavy metals into the water bodies is of great concern. This is because heavy metals are carcinogenic, mutagenic, non-biodegradable, and can accumulate in living organisms causing them to be extremely toxic even at low concentrations [31]. Hence, the removal of these ions from the wastewater before releasing them into the environment is of great importance. From economic and efficiency points of view, adsorption has been regarded as a promising and widely used method for the removal of heavy metals. Thus, the development of adsorbent materials has been crucial to ensure the adsorbent with excellent efficiency and good regeneration toward metal adsorption. In this work, the adsorption efficiency of the samples produced at each stage of fabrication, as well as the final rGO-PDA/Co-ZIF-8 with varying cobalt compositions, was systematically assessed. As an example, the adsorption of Pb(II) with a concentration of 200 mg·L^{-1} at pH 6 was first studied and demonstrated in detail. The initial concentration as well as the concentration of the solution after 5 h of adsorption were analyzed using ICP-OES. The adsorption capacity and removal efficiency were determined by applying Eqs. (1) and (2), respectively. As illustrated in Fig. 6(a), the 3D rGO sample exhibited an adsorption capacity of 365 ± 7.26 mg·g^{-1} with 35% ± 1.07% removal efficiency after 5 h. The main adsorption mechanism involved the interaction of the heavy metal ions with oxygen-containing groups on rGO,

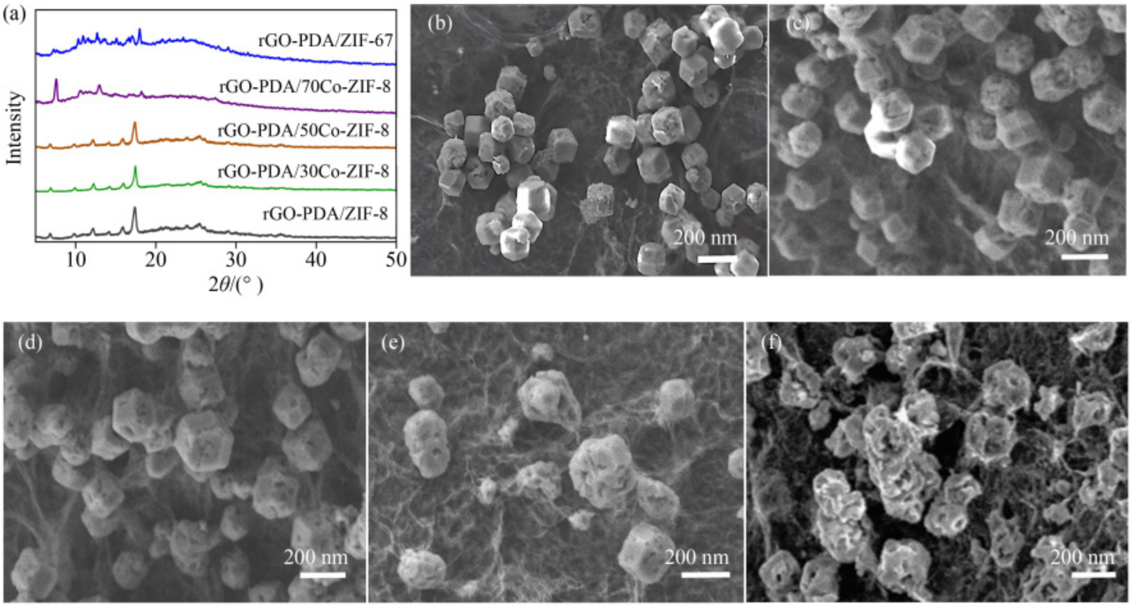

Fig. 5 The characterization of as-synthesized aerogels at various Co doping after ten days immersion in aqueous solution: (a) XRD patterns, and SEM imaging of (b) rGO-PDA/ZIF-8 aerogel, (c) rGO-PDA/30Co-ZIF-8 aerogel, (d) rGO-PDA/50Co-ZIF aerogel, (e) rGO-PDA/70Co-ZIF aerogel, and (f) rGO-PDA/ZIF-67 aerogel.

e.g., the carboxyl groups. As evidenced by FTIR and XPS analyses (see Section 3.3), although the total amount of oxygen content decreased after reduction, a small quantity of carboxyl groups remained in the compact rGO structure, hence, contributing to the overall Pb adsorption. In addition to the presence of oxygen-functional sites, another more prevalent factor contributing to the adsorption of the Pb ions was the existence of C–π electrons on the surface. The rGO acted as a highly reactive Lewis base, capable of donating electron pairs in an aqueous solution. Meanwhile, the heavy metal ions can act as Lewis acids that accept electron pairs further enhancing Lewis acid-base interactions [32]. Furthermore, the exceptional porous structure and specific surface area of the 3D sponge-like structure of rGO also played a crucial role in the enhanced adsorption of heavy metal ions, making it an ideal adsorption candidate with good mechanical stability and more accessible adsorption sites. After the rGO sample underwent PDA functionalization, the adsorption capacity enhanced up to 721 ± 14.42 $\mathrm{mg \cdot g^{-1}}$ alongside a removal efficiency of 67% ± 2.03%. PDA endowed the rGO surface with catechol, aromatic, amines, and imine groups. These groups in PDA with powerful chelating ability served as the active sites for the metal ions through interactions such as electrostatic or chelation, thus, enhancing the adsorption performance [33]. Interestingly, after the *in situ* synthesis of Co-ZIF-8 on the aerogel, a notable increase in adsorption capacity up to 942 ± 18.85 $\mathrm{mg \cdot g^{-1}}$ with a removal efficiency of 87% ± 2.86% was observed. This is because of the affinity of the lead atoms with the nitrogen atom of the 2-methylimidazole. More specifically, the pyridine nitrogen (C=N) and iminium (C–NH) in 2-methylimidazole form a more stable coordination structure with Pb(II) during the adsorption process [34]. Furthermore, the extensive surface area of ZIF-8 nano-adsorbents possessed useful adsorption sites for more Pb(II) ions to be adsorbed via physical interaction (or adsorption forces) [35]. Therefore, the enhancement of the adsorptive capabilities of rGO-PDA/ZIF-8 on Pb ions involved multiple mechanisms, such as electrostatic interactions, surface adsorption, and electron sharing.

The adsorption capacity and removal efficiency were further evaluated for the aerogels with different cobalt-doped concentrations with an initial concentration of 200 $\mathrm{mg \cdot L^{-1}}$ at pH 6. It was observed that the adsorption capacity increased as the amount of cobalt-doped increased (Fig. 6(a)). More precisely, the rGO-PDA/30Co-ZIF-8, rGO-PDA/50Co-ZIF-8, rGO-PDA/70Co-ZIF-8 and rGO-PDA/ZIF-67 exhibits adsorption capacity of 1188 ± 23.77, 1217 ± 24.35, 1235 ± 24.71, 1268 ± 25.32 $\mathrm{mg \cdot g^{-1}}$, respectively. The rGO-PDA/30Co-ZIF-8 exhibited a removal efficiency of 92% ± 2.77%. Further increasing the cobalt content in the aerogels (e.g., rGO-PDA/50Co-

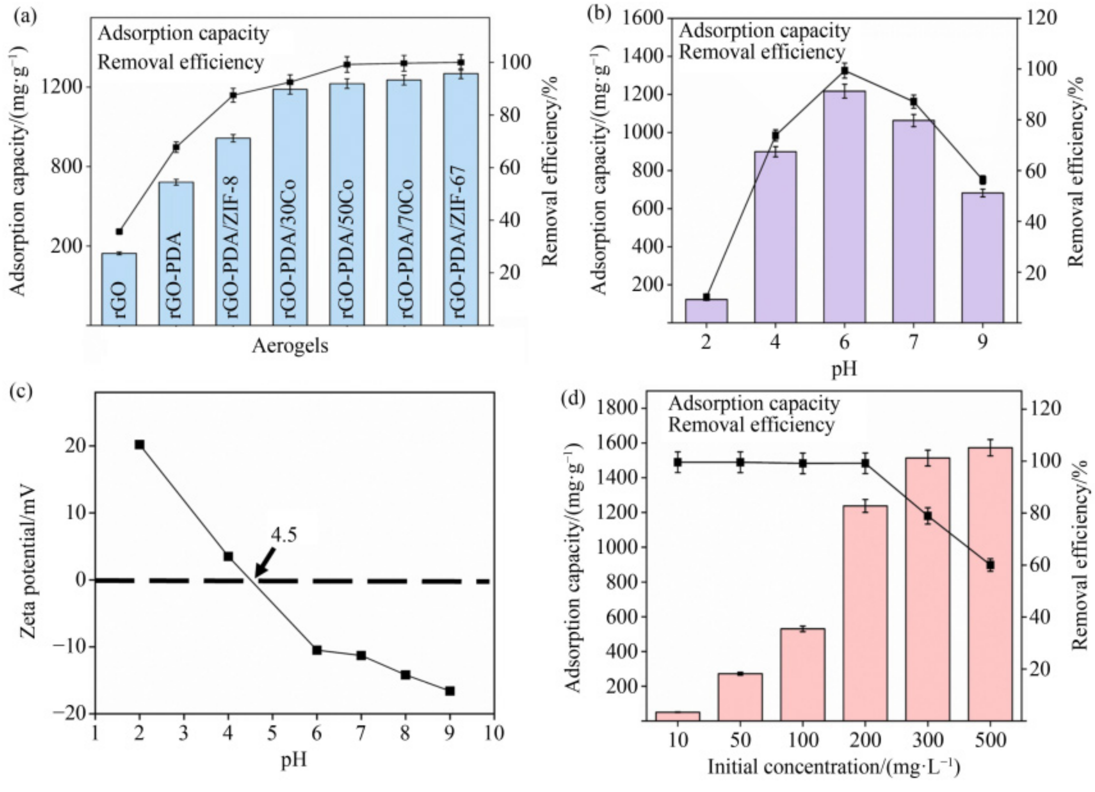

Fig. 6 Heavy metal adsorption performance of the as-synthesized aerogels: (a) adsorption capacity and removal efficiency of different types of aerogels, (b) adsorption capacity and removal efficiency in different pH environments, (c) zeta potential at different pH, and (d) adsorption capacity and removal efficiency at different initial concentrations for 3D rGO-PDA/50-ZIF-8 aerogel.

ZIF-8, rGO-PDA/70Co-ZIF-8, and rGO-PDA/ZIF-67) resulted in a removal efficiency of > 99%. As discussed above, the enhancement in the adsorption performance is not only contributed by the interaction of Pb(II) with 2-methylimidazole but is also substantially influenced by the specific surface area as well as the metal center of ZIFs. It was noticed that the specific surface area increased when the cobalt concentration was increased up to 50%. However, a decrease in specific surface area was observed for the rGO-PDA/70Co-ZIF-8 and rGO-PDA/ZIF-67 aerogels which have higher Co dopings. Interestingly, they showed a slight increase in the adsorption capacity, indicating the importance of the influence of the increased ZIF metal centers on Pb adsorption. The cobalt atoms have a higher affinity than zinc atoms and could easily share electrons with lead atoms due to the nature of the electronic configuration of the elements. More specifically, Pb(II) has only 2 electrons on the *p*-orbitals, while cobalt has more vacant *d*-orbitals [36]. In other to achieve a stable form, these two elements tend to share electrons. On the other hand, the zinc orbital is already occupied with electrons and does not tend to share or donate electrons with other elements. Therefore, the increasing cobalt content in the ZIFs structure could also contribute to the increase in the heavy metal adsorption due to the electron-sharing mechanism.

Extensive research has demonstrated that the pH value of effluent is a crucial factor that significantly affects the performance of adsorbents and is key to the overall adsorption process. Therefore, the behavior of the aerogel under different environmental conditions was evaluated by varying the pH from 2 to 9. Considering the exceptional stability in water, high specific surface area as well high adsorption capacity, the rGO-PDA/50Co-ZIF-8 aerogel was chosen in this study. The adsorption capacity ($mg\cdot g^{-1}$) and removal efficiency (%) of the aerogel were examined at different pH conditions with the initial concentration of the lead solution of 200 $mg\cdot L^{-1}$. As illustrated in Fig. 6(b), the adsorption of lead ions (Pb^{2+}) enhanced as the pH level rose from 2 to 6, followed by a decrease at pH 7 and 9. More specifically, the aerogel exhibited an adsorption capacity of 122 ± 13.13, 899 ± 22.17, 1217 ± 2.19, 1062 ± 17.27, and 682 ± 15.76 $mg\cdot g^{-1}$ at pH = 2, 4, 6, 7, and 9, respectively. Likewise, a similar trend was observed for removal efficiency as the aerogel showed a removal efficiency of 10% ± 1.06%, 73% ± 5.55%, 99% ± 0.1%, 87% ± 1.41%, and 56% ± 2.15% at pH 2, 4, 6, 7, and 9, respectively. The effect of pH can be explained by the speciation of adsorbates and the surface charge density of the adsorbent across different pH levels. Heavy metals, particularly lead ions (Pb^{2+}), could stably stay in the solution as a positively charged ion in the studied pH range [37]. Figure 6(c) displayed the surface charge of rGO-PDA/50Co-ZIF-8 aerogel from zeta potential analysis. Notably, the increase of pH from 2 to 11 showed a reduction in the material zeta potential. This can be attributed to the deprotonation of functional groups present in the rGO and PDA at higher pH [35]. The aerogel exhibited an isoelectric point of 4.5, which indicates that the aerogel has a positive surface charge at pHs below 4.5 and a negative surface charge at pHs above 4.5. In particular, when the pH was below 4.5, the rGO-PDA/ZIF-8 aerogel's surface became positively charged because of the protonation of PDA's phenolic groups and the destabilization of Co-ZIF-8 crystals under acidic conditions [38]. On the other hand, in highly acidic conditions, a high concentration of H^+ could compete with Pb(II) on the surface adsorption sites, leading to a lower adsorption capacity and removal efficiency [39]. On the other hand, when the pH exceeded 4.0, the surface charge shifted to a more negative state as a result of the deprotonation of the phenolic groups in PDA. Concurrently, the Co-doped ZIF-8 crystals exhibited a negative charge, offering additional sites for adsorption [40]. Thus, the electrostatic attractions between the aerogel's sites and Pb(II) further enhanced the adsorption capacity and removal efficiency. Furthermore, the concentration of H^+ decreased, and the competition between Pb(II) and H^+ weakened leading to the enhancement of adsorption capacity [41]. However, at higher pH values (pH > 6.0), the aerogel exhibited a decrease in adsorption capacity and removal efficiency due to the formation of $Pb(OH)_2$ in the solution that might compete with the adsorbent, leading to a deterioration of the adsorption performance [16].

To explore the maximum adsorption capability of the rGO-PDA/50Co-ZIF-8 aerogel for Pb(II), the concentration of Pb(II) was adjusted between 10 and 500 $mg\cdot L^{-1}$ at pH = 6, and both the adsorption capacity ($mg\cdot g^{-1}$) and the efficiency of removal (%) were assessed. As the concentration of Pb(II) ions increases from 10 to 200 $mg\cdot L^{-1}$, the adsorption capacity increased from 50 ± 1.51 to 1237 ± 37.41 $mg\cdot g^{-1}$ with a removal efficiency of > 99% (Fig. 6(d)). This increase in adsorption capacity is attributed to the enhanced driving force provided by the higher concentrations of Pb(II) ions, which, in turn, accelerates the mass transfer between the Pb(II) ions and the aerogel [42]. However, only a slight increase in adsorption capacity from 1513 ± 45.41 to 1573 ± 47.19 $mg\cdot g^{-1}$ was noted, as the pH increased from 300 to 500 $mg\cdot L^{-1}$. This suggested that the rGO-PDA/50Co-ZIF-8 aerogel reached its highest adsorption capacity at 1573 ± 1.18 $mg\cdot g^{-1}$ as all adsorptive sites became occupied by Pb(II) ions. Nonetheless, the efficiency of removal reduced to 75% ± 3.03% and 58% ± 2.32% for initial concentrations of 300 and 500 $mg\cdot L^{-1}$, respectively. This was because of the presence of excess Pb(II) ions in the solution, and then the adsorption sites became saturated easily and quickly, thus showing a decreased removal efficiency. Additionally, the rGO-PDA/50Co-

ZIF-8 aerogel shows good adsorption performance toward other types of heavy metals such as Cu(II) and Cd(II). Notably, it exhibits the highest removal efficiency of ~99% for Pb(II), followed by ~95% for Cu(II) and ~92% for Cd(II) (refer to Fig. S7, cf. ESM). In comparison with previous studies (Table S4, cf. ESM), it becomes evident that this particular aerogel has demonstrated an exceptionally high adsorption capacity across the entire range of heavy metals that were tested. In addition, it was found that the concentration of cobalt and zinc can be negligible, which indicates there was no leaching during the adsorption process. These findings underscore the significance of this aerogel in the field of heavy metal adsorption and emphasize its potential as a superior solution for effectively and comprehensively addressing heavy metal contamination in various environmental and industrial contexts.

The evaluation of adsorbent selectivity is important considering different situations in real applications. For instance, in cases where wastewater is contaminated with various heavy metal ions, a preference is given to less selective adsorbents. Conversely, when specific heavy metal ions are identified as contaminants in wastewater, selective adsorbents are deemed more appropriate. Hence, the selectivity of the rGO-PDA/Co-ZIF-8 aerogel was evaluated by subjecting it to the aqueous solution containing mixed heavy metal ions such as Pb^{2+}, Cd^{2+}, Cu^{2+}, Mg^{2+}, and Na^{2+} with the initial concentrations of 0.6 $mmol \cdot L^{-1}$ at pH 6. It was found that the aerogel exhibited adsorption selectivity in the order Pb(II) > Cu(II) > Cd(II) > Mg(II) > Na^+ with the adsorption capacity of 634 ± 15.2, 327 ± 20.4, 156 ± 20.4, 72 ± 10.8, and 21 ± 8.9 $mg \cdot g^{-1}$, respectively (Fig. S8, cf. ESM). The variations in adsorption capacity exhibited by the rGO-PDA/Co-ZIF-8 aerogel for different heavy metals stem from the distinct binding abilities of the functional groups present on the aerogel. Hence, it has been proposed that aerogel exhibits promising potential in the removal of diverse heavy metal ions from wastewater.

3.5.2 Adsorption kinetics and adsorption isotherm

In this research, the fundamental adsorption process was examined through the use of relevant kinetic models. The investigation employed two models, namely the PFO and PSO, to evaluate how Pb(II) adsorbs onto the rGO-PDA/50Co-ZIF-8 aerogel. Equation (3), which outlines the PFO model, is frequently applied in the analysis of solutes at low concentrations. Conversely, the PSO model, detailed in Eq. (4), relies on the quantity of the substance adsorbed on the surface [43].

Consequently, a detailed kinetic analysis was conducted for different initial concentrations of Pb(II) ions using the PFO and PSO models. Figures 7(a) and 7(b) illustrate the use of these models along with linear-fitting curves for diverse concentrations of Pb(II) ions. The adsorption kinetic parameters and correlation coefficients calculated by fitting the kinetic equation are shown in Table 1. As can be seen from Figs. 7(a) and 7(b) and Table 1, the fitting results indicated that the PSO kinetic model (R^2 = 0.999) can preferably describe the adsorption kinetics behavior of the rGO-PDA/50Co-ZIF-8 aerogel.

Therefore, chemical adsorption may be the rate-limiting step in the adsorption process that involves electron covalent or electron migration between adsorbent and adsorbates [44]. In addition, the experimental $q_{e,exp}$, and calculated $q_{e,cal}$ values of the equilibrium adsorption capacity showed a huge difference, suggesting that the adsorption of Pb(II) on the rGO-PDA/50Co-ZIF-8 aerogel did not conform to the PFO model. Instead, the PSO model showed a good fit with experimental data for all initial concentrations. The values of $q_{e,cal}$ also appeared to be very close to the experimentally observed values of $q_{e,exp}$. These results further suggested that the adsorption kinetics followed the PSO model. It was also observed that as the initial concentration increased from 10 to 500 $mg \cdot L^{-1}$, the values of $q_{e,cal}$ increased from 50 ± 1.68 to 1573 ± 1.18 $mg \cdot g^{-1}$. This is because, at a high initial concentration, the relative driving force of the concentration gradient is strong. Meanwhile, the decrease in K_2 value from 1.5×10^{-3} to 6.4×10^{-6} $g \cdot mg^{-1} \cdot min^{-1}$ was due to the lower competition for the adsorption sites at lower concentrations. Similar phenomena were also observed in other studies on the adsorption of heavy metal ions [45,46].

In this work, Langmuir and Freundlich's isotherms were used to probe the interaction mechanism between the adsorbent and Pb(II). The Langmuir model is suitable for describing monolayer adsorption of homogenous solid structures where all adsorption sites are identical and the particles being adsorbed have no interaction with each other and are completely independent [47]. The Freundlich model is an empirical equation with no assumptions and is suitable for describing non-homogenous multilayer adsorption with different adsorption sites [48]. The adsorption isotherm models of Langmuir and Freundlich are represented in Eqs. (5) and (6). Figures 7(c) and 7(d) showed the fitting results for Langmuir and Freundlich isotherm models, respectively. As shown in Table S4, the correlation coefficient of the Langmuir model (R^2 = 0.999) is much larger than that of the Freundlich model (R^2 = 0.7532), which suggests that the adsorption of Pb(II) on the rGO-PDA/50-ZIF-8 aerogel complied to a single-layer process due to the uniform allocation of available groups on the rGO-PDA surface and as well as on the bimetallic ZIFs.

3.5.3 Potential adsorption mechanism

As illustrated in Fig. 8, the adsorption mechanism of 3D rGO-PDA/Co-ZIF-8 aerogel was mainly governed by

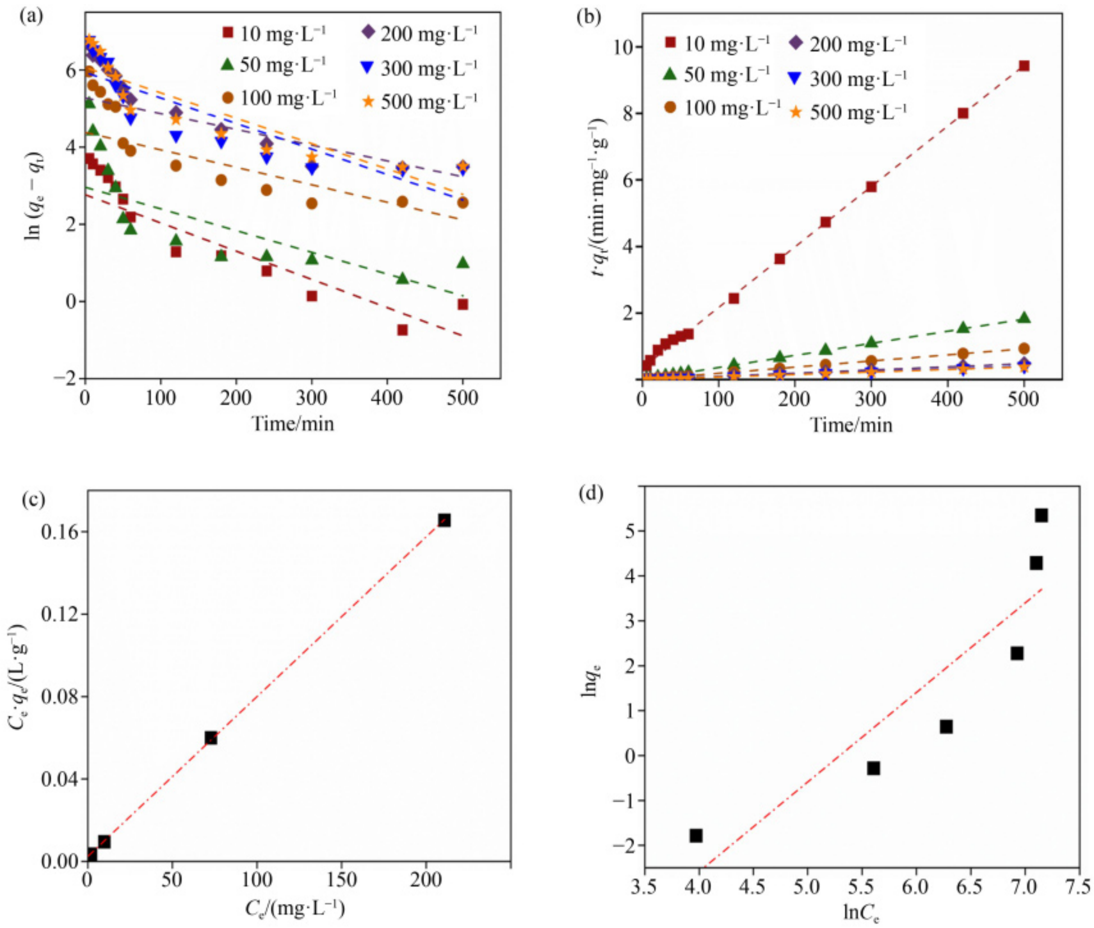

Fig. 7 Adsorption kinetics of rGO-PDA/50Co-ZIF-8: (a) PFO model, and (b) PSO model. Adsorption isotherm of rGO-PDA/50Co-ZIF-8: (c) Langmuir model, and (d) Freundlich model at initial concentration of 10, 50, 100, 200, 300, 500 mg·L^{-1}.

Table 1 Kinetic parameters for different concentrations of lead

Kinetic model	Parameter	10/(mg·L^{-1})	50/(mg·L^{-1})	100/(mg·L^{-1})	200/(mg·L^{-1})	300/(mg·L^{-1})	500/(mg·L^{-1})
PFO	K_1/min^{-1}	-4×10^{-5}	-1.4×10^{-5}	-1.4×10^{-5}	-1.8×10^{-5}	-1.6×10^{-5}	-1.3×10^{-5}
	$q_{e,cal}$/(mg·g^{-1})	2.31	176.17	611.66	2150.87	2275.37	1570.95
	R^2	0.1024	0.7135	0.8107	0.8909	0.8131	0.9580
PSO	K_2/(g·mg^{-1}·min^{-1})	1.5×10^{-3}	2.5×10^{-5}	3.7×10^{-5}	3.9×10^{-6}	4.5×10^{-6}	6.4×10^{-6}
	$q_{e,cal}$/(mg·g^{-1})	33.76	369.00	787.40	1214.68	1485.42	1439.99
	R^2	0.9912	0.9952	0.9989	0.9997	0.9951	0.9998

electrostatic attractions, complexation, and electron sharing. Each component in the composite aerogel played an important role in the adsorption of lead. First, Pb(II) can be adsorbed onto the porous structure of rGO from the aqueous solutions via two pathways, i.e., a complexation reaction between the Pb(II) and the electron on the π-bond in the rGO. rGO can easily donate electrons from its π-bond and the outer orbital of Pb could accept the electron cloud from the outside, thus forming a complexation bond. Second, the Pb(II) prefers to bind with the C–OH groups on the rGO via electrostatic interaction [49]. Upon the modification with PDA, the aerogel was endowed with abundant functional groups such as catechol, amine, and phenyl groups which could serve as the active sites for ZIF nucleation as well as the adsorption of Pb(II) via electrostatic interactions and metal coordination [50]. The Co-doped ZIF-8 nanocrystals that were decorated on the surface of rGO-PDA aerogels, provide a significantly higher surface area for the adsorption of Pb(II) because of its strong affinity toward the nitrogen atom in the ZIF structure, forming a stable chelation on the crystal external surface. In addition, the presence of cobalt in the structure of ZIF nanocrystals could further increase the affinity toward Pb(II), because the cobalt and Pb(II) tend to share electrons (the two electrons on the outer shell of Pb(II)

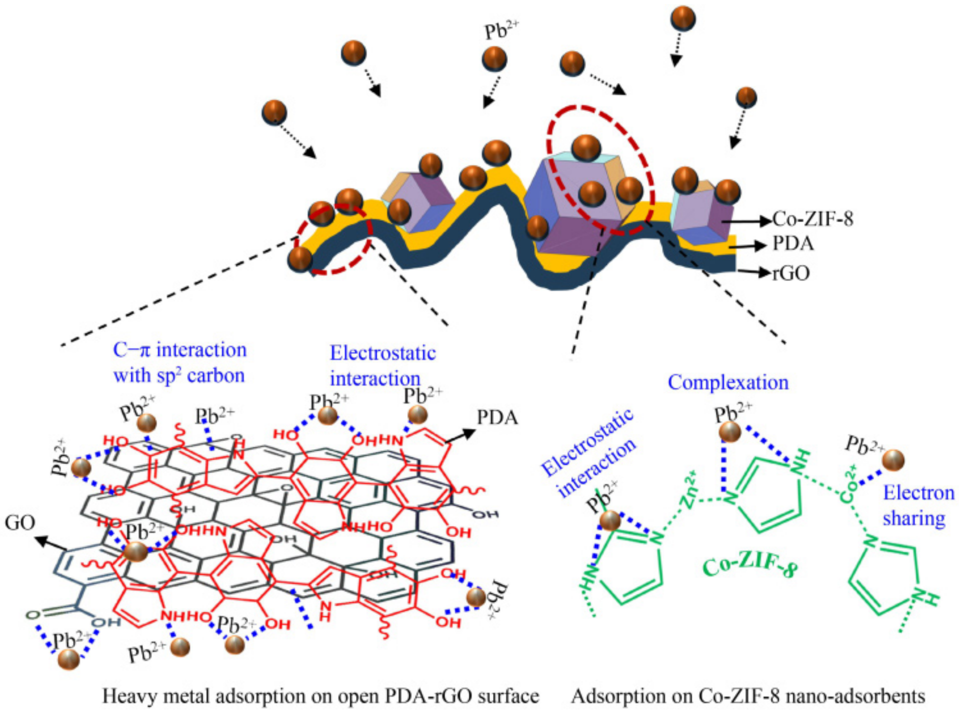

Fig. 8 Illustration of Pb(II) adsorption mechanism on rGO-PDA/50Co-ZIF-8 aerogel.

tend to fill the vacant in the *d*-orbital of cobalt, forming a stable bond).

3.6 Regeneration and cyclic adsorption performance

Considering the environmental safety and economic feasibility, an adsorbent must show a reasonable number of cycles during the adsorption. The long-term performance of rGO-PDA/50Co-ZIF-8 aerogel was evaluated via cyclic adsorption. To regenerate the aerogel, 0.05 mol·L^{-1} HNO_3 was used as a stripping agent and sequentially washed with copious deionized water until the final eluent reached neutral pH. In this work, at least 7 cycles of adsorption-regeneration were tested on the same rGO-PDA/50Co-ZIF-8 aerogel. As shown in Fig. 9(a), after seven cycles, the aerogel still showed a stable 1023 ± 20.5 mg·g^{-1} and removal efficiency of ~84%. The EDX spectra analysis of the aerogels following seven cycles of adsorption demonstrated the absence of Pb, indicating the efficacy of the washing step in effectively removing heavy metal ions from the aerogel (Fig. 9(b)). The SEM analysis showed that the aerogel still maintained a good structure with intact ZIF nanocrystals, indicating their excellent stability and useful for long-term performance (Fig. 9(c)). The localized EDS mapping of Zn and Co on the sample after seven cycles again showed that the elements were well distributed in the crystal structure (Figs. 9(d–f)). It is worth mentioning that the presence of Zn and Co in the aerogel underscores robust and enduring crystal adherence to the aerogel structure, mitigating the risk of potential metal leaching during the adsorption treatment.

4 Conclusions

In conclusion, a highly efficient adsorbent, rGO-based aerogel functionalized with PDA and cobalt-doped crystals, was successfully fabricated. The synthesis strategy involved the self-assembling of rGO to form a highly porous 3D network structure, followed by surface PDA modification and *in situ* crystallization of the cobalt-doped crystals in the aerogel structure. The surface properties as well as the structural hydrostability can be controlled via Co-doping. For example, rGO-PDA/50Co-ZIF-8 exhibited the highest surface area of 900 m^2·g^{-1} and the best structural integrity even after ten days of immersion in water. In addition, abundant surface functional groups and unsaturated cobalt sites in the rGO-PDA/50Co-ZIF-8 enabled rapid and effective adsorbing of heavy metal ions from an aqueous solution. Particularly for Pb(II), an outstanding adsorption capacity of 1217 ± 24.35 mg·g^{-1} and removal efficiency of > 99% were achieved in this work, much more than other aerogel adsorbents. The adsorption mechanism between the aerogel and Pb(II) was studied mainly related to the electrostatic attractions, complexation, and electron sharing. Finally, the aerogels can be easily recycled from water and maintain a stable adsorption capacity of 1023 ± 20.5 mg·g^{-1} with a removal efficiency of ~84%, suggesting their great potential in the high-capacity heavy metals removal from industrial effluents.

Competing interests The authors declare that they have no competing interests.

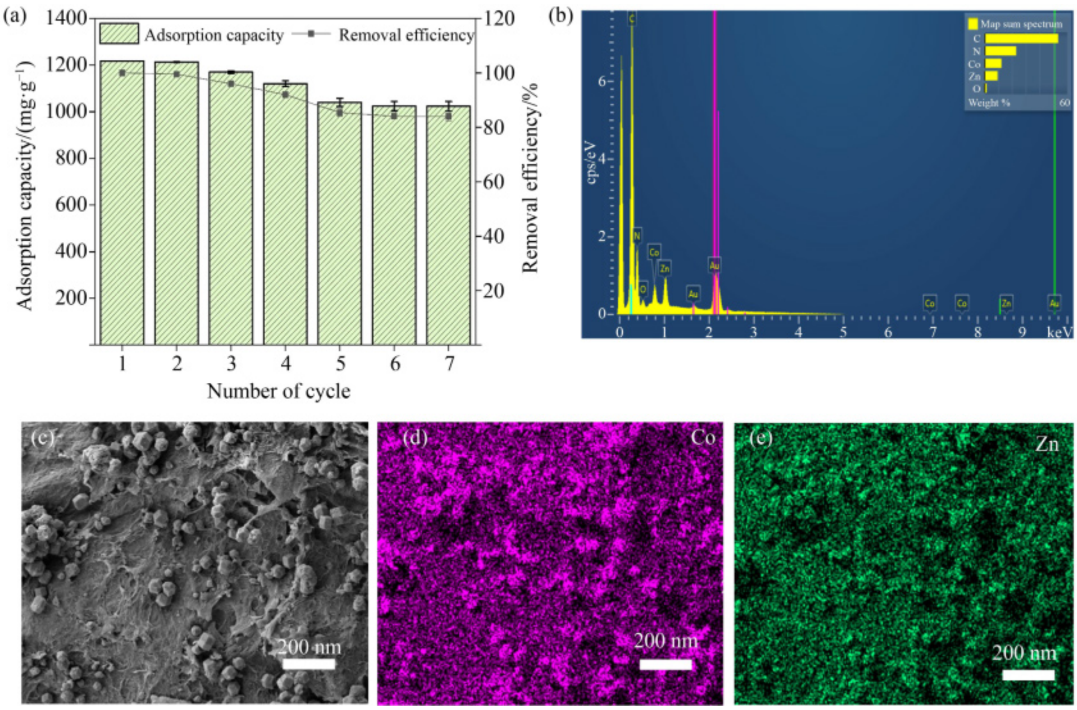

Fig. 9 Regeneration of rGO-PDA/50Co-ZIF-8 aerogel: (a) cyclic adsorption performance, (b) EDX spectra, (c) SEM imaging, and (d, e) EDS mapping of Co and Zn after 7 cycles of adsorption.

Acknowledgements This work was funded by Jiangsu Dingying New Materials Co., Ltd. under Grant Number (C-00005685) and the School of Engineering, the University of Edinburgh. N.A.M. acknowledges the Malaysian Government for awarding a Ph.D. scholarship. The authors would like to thank Fergus Dingwall for his laboratory assistance and we acknowledge the use of the Zeiss Crossbeam Cryo FIB/SEM bought with the EPSRC grant EP/P030564/1 and Fraser Laidlaw for help with image acquisition.

Electronic Supplementary Material Supplementary material is available in the online version of this article at https://dx.doi.org/10.1007/s11705-024-2442-0 and is accessible for authorized users.

Funding note Funding note not available.

References

1. Azimi A, Azari A, Rezakazemi M, Ansarpour M. Removal of heavy metals from industrial wastewaters: a review. ChemBioEng Reviews, 2017, 4(1): 37–59
2. Zou Y, Wang X, Khan A, Wang P, Liu Y, Alsaedi A, Hayat T, Wang X. Environmental remediation and application of nanoscale zero-valent iron and its composites for the removal of heavy metal ions: a review. Environmental Science & Technology, 2016, 50(14): 7290–7304
3. Li X, Wang B, Cao Y, Zhao S, Wang H, Feng X, Zhou J, Ma X. Water contaminant elimination based on metal-organic frameworks and perspective on their industrial applications. ACS Sustainable Chemistry & Engineering, 2019, 7(5): 4548–4563
4. Mariana M, Abdul A K, Mistar E M, Yahya E B, Alfatah T, Danish M, Amayreh M. Recent advances in activated carbon modification techniques for enhanced heavy metal adsorption. Journal of Water Process Engineering, 2021, 43: 102221
5. Rahman N S A, Yhaya M F, Azahari B, Ismail W R. Utilisation of natural cellulose fibres in wastewater treatment. Cellulose (London, England), 2018, 25(9): 4887–4903
6. Ihsanullah I, Sajid M, Khan S, Bilal M. Aerogel-based adsorbents as emerging materials for the removal of heavy metals from water: progress, challenges, and prospects. Separation and Purification Technology, 2022, 291: 120923
7. Chandra V, Park J, Chun Y, Lee J W, Hwang I C, Kim K S. Water-dispersible magnetite-reduced graphene oxide composites for arsenic removal. ACS Nano, 2010, 4(7): 3979–3986
8. Stankovich S, Piner R D, Chen X, Wu N, Nguyen S T, Ruoff R S. Stable aqueous dispersions of graphitic nanoplatelets via the reduction of exfoliated graphite oxide in the presence of poly(sodium 4-styrenesulfonate). Journal of Materials Chemistry, 2006, 16(2): 155–158
9. Xu Y, Wu Q, Sun Y, Bai H, Shi G. Three-dimensional self-assembly of graphene oxide and DNA into multifunctional hydrogels. ACS Nano, 2010, 4(12): 7358–7362
10. Chen T, Wei X, Chen Z, Morin D, Alvarez S V, Yoon Y, Huang

Y. Designing energy-efficient separation membranes: Knowledge from nature for a sustainable future. Advanced Membranes, 2022, 2: 100031

11. Muschi M, Serre C. Progress and challenges of graphene oxide/metal-organic composites. Coordination Chemistry Reviews, 2019, 387: 262–272
12. Saliba D, Ammar M, Rammal M, Al-Ghoul M, Hmadeh M. Crystal growth of ZIF-8, ZIF-67, and their mixed-metal derivatives. Journal of the American Chemical Society, 2018, 140(5): 1812–1823
13. Kaur G, Rai R K, Tyagi D, Yao X, Li P Z, Yang X C, Zhao Y, Xu Q, Singh S K. Room-temperature synthesis of bimetallic Co-Zn based zeolitic imidazolate frameworks in water for enhanced CO_2 and H_2 uptakes. Journal of Materials Chemistry. A, Materials for Energy and Sustainability, 2016, 4(39): 14932–14938
14. Zaręba J K, Nyk M, Samoć M. Co/ZIF-8 heterometallic nanoparticles: control of nanocrystal size and properties by a mixed-metal approach. Crystal Growth & Design, 2016, 16(11): 6419–6425
15. Mazlan N A, Butt F S, Lewis A, Krishnamoorthi R, Chen S, Radacsi N, Huang Y. Robust reduced graphene oxide-PDA/ZIF-8 aerogel composite for cyclic, high-capacity dye adsorption. Separation and Purification Technology, 2024, 334: 126005
16. Yang Q, Lu R, Ren S S, Chen C, Chen Z, Yang X. Three dimensional reduced graphene oxide/ZIF-67 aerogel: effective removal cationic and anionic dyes from water. Chemical Engineering Journal, 2018, 348: 202–211
17. Tang L, Dang J, He M, Li J, Kong J, Tang Y, Gu J. Preparation and properties of cyanate-based wave-transparent laminated composites reinforced by dopamine/POSS functionalized Kevlar cloth. Composites Science and Technology, 2019, 169: 120–126
18. Chen T, Butt F S, Zhang M, Wei X, Lewis A, Radacsi N, Semiao A J C, Han J, Huang Y. Ultra-permeable zeolitic imidazolate frameworks-intercalated graphene oxide membranes for unprecedented ultrafast molecular separation. Chemical Engineering Journal, 2021, 419: 129507
19. Huang H H, De Silva K K H, Kumara G R A, Yoshimura M. Structural evolution of hydrothermally derived reduced graphene oxide. Scientific Reports, 2018, 8(1): 6849
20. Xi Z Y, Xu Y Y, Zhu L P, Wang Y, Zhu B K. A facile method of surface modification for hydrophobic polymer membranes based on the adhesive behavior of poly(DOPA) and poly(dopamine). Journal of Membrane Science, 2009, 327(1–2): 244–253
21. Luan Tran B, Chin H Y, Chang B K, Chiang A S. Dye adsorption in ZIF-8: the importance of external surface area. Microporous and Mesoporous Materials, 2019, 277: 149–153
22. Ren H, Kulkarni D D, Kodiyath R, Xu W, Choi I, Tsukruk V V. Competitive adsorption of dopamine and rhodamine 6G on the surface of graphene oxide. ACS Applied Materials & Interfaces, 2014, 6(4): 2459–2470
23. Maharsi R, Arif A F, Ogi T, Widiyandari H, Iskandar F. Electrochemical properties of TiO_x/rGO composite as an electrode for supercapacitors. RSC Advances, 2019, 9(48): 27896–27903
24. Han X, Zhang L, Li C. Preparation of polydopamine-functionalized graphene-Fe_3O_4 magnetic composites with high adsorption capacities. RSC Advances, 2014, 4(58): 30536–30541
25. Abuzalat O, Tantawy H, Basuni M, Alkordi M H, Baraka A. Designing bimetallic zeolitic imidazolate frameworks (ZIFs) for aqueous catalysis: Co/Zn-ZIF-8 as a cyclic-durable catalyst for hydrogen peroxide oxidative decomposition of organic dyes in water. RSC Advances, 2022, 12(10): 6025–6036
26. Zou R, Liu F, Hu N, Ning H, Jiang X, Xu C, Fu S, Li Y, Zhou X, Yan C. Carbonized polydopamine nanoparticle reinforced graphene films with superior thermal conductivity. Carbon, 2019, 149: 173–180
27. Zhao M, Tesfay Reda A, Zhang D. Reduced graphene oxide/ZIF-67 aerogel composite material for uranium adsorption in aqueous solutions. ACS Omega, 2020, 5(14): 8012–8022
28. Liu Y, Fu J, He J, Wang B, He Y, Luo L, Wang L, Chen C, Shen F, Zhang Y. Synthesis of a superhydrophilic coral-like reduced graphene oxide aerogel and its application to pollutant capture in wastewater treatment. Chemical Engineering Science, 2022, 260: 117860
29. Park H, Amaranatha Reddy D, Kim Y, Ma R, Choi J, Kim T K, Lee K S. Zeolitic imidazolate framework-67 (ZIF-67) rhombic dodecahedrons as full-spectrum light harvesting photocatalyst for environmental remediation. Solid State Sciences, 2016, 62: 82–89
30. Zhu G, Li H, Deng S, Zhang C, Kang K, Zhang X, Li K. *In situ* growth of bimetallic Co/Zn-ZIF within wood scaffold for enhanced adsorption capacity and improved flame retardancy. Wood Science and Technology, 2022, 56(6): 1657–1673
31. Kobielska P A, Howarth A J, Farha O K, Nayak S. Metal-organic frameworks for heavy metal removal from water. Coordination Chemistry Reviews, 2018, 358: 92–107
32. Nundy S, Ghosh A, Nath R, Paul A, Tahir A A, Mallick T K. Reduced graphene oxide (rGO) aerogel: efficient adsorbent for the elimination of antimony (III) and (V) from wastewater. Journal of Hazardous Materials, 2021, 420: 126554
33. Ha Y M, Kim Y N, Jung Y C. Rapid and local self-healing ability of polyurethane nanocomposites using photothermal polydopamine-coated graphene oxide triggered by near-infrared laser. Polymers, 2021, 13(8): 1274
34. Wang L, Zhao X, Zhang J, Xiong Z. Selective adsorption of Pb(II) over the zinc-based MOFs in aqueous solution-kinetics, isotherms, and the ion exchange mechanism. Environmental Science and Pollution Research International, 2017, 24(16): 14198–14206
35. Yang W, Kong Y, Yin H, Cao M. Study on the adsorption performance of ZIF-8 on heavy metal ions in water and the recycling of waste ZIF-8 in cement. Journal of Solid State Chemistry, 2023, 326: 124217
36. Ahmad K, Ashfaq M, Shah S S A, Hussain E, Naseem H A, Parveen S, Ayub A. Effect of metal atom in zeolitic imidazolate frameworks (ZIF-8 & 67) for removal of Pb^{2+} & Hg^{2+} from water. Food and Chemical Toxicology, 2021, 149: 112008
37. Yu C X, Wang K Z, Li X J, Liu D, Ma L F, Liu L L. Highly efficient and facile removal of Pb^{2+} from water by using a negatively charged azoxy-functionalized metal-organic framework. Crystal Growth & Design, 2020, 20(8): 5251–5260
38. Ighalo J O, Rangabhashiyam S, Adeyanju C A, Ogunniyi S, Adeniyi A G, Igwegbe C A. Zeolitic imidazolate frameworks

(ZIFs) for aqueous phase adsorption—a review. Journal of Industrial and Engineering Chemistry, 2022, 105: 34–48

39. Gao C, Dong Z, Hao X, Yao Y, Guo S. Preparation of reduced graphene oxide aerogel and its adsorption for Pb(II). ACS Omega, 2020, 5(17): 9903–9911
40. Nazir M A, Najam T, Shahzad K, Wattoo M A, Hussain T, Tufail M K, Shah S S A, Rehman A. Heterointerface engineering of water stable ZIF-8@ZIF-67: adsorption of rhodamine B from water. Surfaces and Interfaces, 2022, 34: 102324
41. Chen H, Li T, Zhang L, Wang R, Jiang F, Chen J. Pb(II) adsorption on magnetic γ-Fe_2O_3/titanate nanotubes composite. Journal of Environmental Chemical Engineering, 2015, 3(3): 2022–2030
42. Scheufele F B, Módenes A N, Borba C E, Ribeiro C, Espinoza-Quiñones F R, Bergamasco R, Pereira N C. Monolayer-multilayer adsorption phenomenological model: kinetics, equilibrium and thermodynamics. Chemical Engineering Journal, 2016, 284: 1328–1341
43. Bulut E, Özacar M, Şengil I A. Adsorption of malachite green onto bentonite: equilibrium and kinetic studies and process design. Microporous and Mesoporous Materials, 2008, 115(3): 234–246
44. Zubair Y O, Fuchida S, Tokoro C. Insight into the mechanism of arsenic(III/V) uptake on mesoporous zerovalent iron-magnetite nanocomposites: adsorption and microscopic studies. ACS Applied Materials & Interfaces, 2020, 12(44): 49755–49767
45. Zhao C, Hong P, Li Y, Song X, Wang Y, Yang Y. Mechanism of adsorption of tetracycline-Cu multi-pollutants by graphene oxide (GO) and reduced graphene oxide (rGO). Journal of Chemical Technology and Biotechnology, 2019, 94(4): 1176–1186
46. Zeng Q, Qi X, Zhang M, Tong X, Jiang N, Pan W, Xiong W, Li Y, Xu J, Shen J, et al. Efficient decontamination of heavy metals from aqueous solution using pullulan/polydopamine hydrogels. International Journal of Biological Macromolecules, 2020, 145: 1049–1058
47. Foo K Y, Hameed B H. Insights into the modeling of adsorption isotherm systems. Chemical Engineering Journal, 2010, 156(1): 2–10
48. Saadi R, Saadi Z, Fazaeli R, Fard N E. Monolayer and multilayer adsorption isotherm models for sorption from aqueous media. Korean Journal of Chemical Engineering, 2015, 32(5): 787–799
49. Zhang Y, Cao B, Zhao L, Sun L, Gao Y, Li J, Yang F. Biochar-supported reduced graphene oxide composite for adsorption and coadsorption of atrazine and lead ions. Applied Surface Science, 2018, 427: 147–155
50. Liu Y, Ai K, Lu L. Polydopamine and its derivative materials: synthesis and promising applications in energy, environmental, and biomedical fields. Chemical Reviews, 2014, 114(9): 5057–5115